RSC Advances

PAPER

View Article Online
View Journal | View Issue

Cite this: *RSC Adv.*, 2015, **5**, 17300

# One-phonon sideband and multiphonon relaxation in $La_{1.6}Mo_2O_9$: $Eu_{0.4}^{3+}$ and β-$NaGdF_4$: $Tb^{3+}$ nanocrystals

Chunxu Liu,* Jisen Zhang and Yongshi Luo

Received 16th January 2015
Accepted 23rd January 2015

DOI: 10.1039/c5ra00912j

www.rsc.org/advances

The experimental studies of one-phonon sideband (PSB) and multiphonon relaxation (MR), involving a large energy gap (5800 $cm^{-1}$) crossover from bulk to a nanocrystal (NC) system are reported. Two one-phonon sidebands, $PSB_1 = 449$ nm and $PSB_2 = 429$ nm associated with the $Eu^{3+}$ $^7F_0 \rightarrow {}^5D_2$ 464 nm zero phonon line (ZPL), were observed in the excitation spectra monitoring $Eu^{3+}$ $^5D_0 \rightarrow {}^7F_2$ at 613 nm, which resulted from Mo–O and O–Mo–O local mode vibrations, respectively. The phonon densities of states of $\rho(\omega)$ were determined from the profile of PSB. The temperature dependence of MR rate for the $Tb^{3+}$ $^5D_3 \rightarrow {}^5D_4$ in β-$NaGdF_4$:$Tb^{3+}$ NCs was analyzed in a single-frequency approximation of the phonon spectrum in the framework of the nonlinear theory of MR. The experimental data were in good agreement with the theoretical curves within the range of 12 K to 312 K. It is concluded that the MR occurs predominantly *via* high-energy optical phonons.

## Introduction

It is well known that phonons play an important role in luminescence spectroscopy, excited state relaxation and energy-transfer processes.[1–5] Furthermore, experimental results and subsequent analysis on the relaxation dynamics between the various excited levels of rare-earth (RE) ions suggest that two different groups in regards to spatial localization, *i.e.*, one of them represents phonons of the normal unperturbed lattice and the other is a localized mode involved in the process. There is a large difference between the local electron states and the electron states of the free atoms. The interactions between the local electron states and the surrounding atoms in the lattice sites result in more or less the shift of the equilibration position of atoms, or the local electron states lead to the distortion of lattices, which is so-called lattice relaxation.

The electron–phonon interaction arises because the full wave function of the system depends on the positions of the electrons and the ions. When an electronic transition occurs, we have a change in the equilibrium position of the ions around the impurity and this is expressed as an interaction between electrons and ions. In the case of weak electron–phonon interactions, *i.e.* at small Huang–Rhys factor $S$ ($S \leq 1$), the intense zero phonon line (ZPL) and the accompanying weak phonon sideband associated mainly with one-phonon transitions, as can be seen in the spectrum. At large $S$ ($S > 5$),[6] *i.e.* in the case of strong electron–phonon interactions, the intensity of the ZPL is very small, and only a broad phonon band associated with the multiphonon transitions can be seen in the spectrum. Based on the single-configuration-coordinate (SCC) model,[7–10] the profile of the phonon sideband (PSB) was analyzed by Jia, Brundage and Yen[10] in the strong electron–phonon interaction case ($S = 9.5$ and 9.7). To date, only a few studies have been published, which investigates the one phonon sideband in the weak electron–phonon interaction case ($S < 1$)[11] and little attention is paid to the relationship between the profile $I(\omega)$ of the phonon sideband and the phonon density of states $\rho(\omega)$.

The 4f orbitals of the rare earth ion do not form many bonds, and they lie within the energy gap. Furthermore, since the rare earth' 4f orbitals are shielded by the outer $5s^2$ and $5p^6$ orbitals, they are hardly affected by the ligand, which belongs to the weak interaction case. Since widespread applications (such as lighting and displays) depend on the interaction between the 4f electrons and the surroundings atoms, it is justified to investigate the vibronic transitions of the rare earth ions.

The ultraviolet (UV) emission from a GaN-based light emitting diode (LED) can be very efficiently absorbed by the Mo–O charge transfer bands in molybdates. When doping $Eu^{3+}$ into the molybdates, the excitation energy can be transferred to the activator ions $Eu^{3+}$ nonradiatively, resulting in the red emission of $Eu^{3+}$.[12–14] In recent years, molybdate compounds have gained much attention due to their negative thermal expansion (NTE) properties.[15–17] Their facile synthesis and chemical stability make the molybdate compounds good hosts for a dopant.

The serial samples ($d = 4.7$, 56.0 and 115.5 nm) of β-$NaGdF_4$ were synthesized. As for the β-phase $NaGdF_4$, there are three different cation sites in the lattice, *i.e.*, 1a, 1f, and 2h, among which 2h sites are normally occupied by only sodium ions, and

*State Key Laboratory of Luminescence and Applications, Changchun Institute of Optics, Fine Mechanics and Physics, Chinese Academy of Sciences, Changchun 130033, P. R. China. E-mail: cxliu@ciomp.ac.cn*

1a and 1f sites are occupied by $Ln^{3+}$ ions. The β-phase is more ordered and thermodynamically stable. The β-phase of $NaGdF_4$ is more suitable as a matrix of down and up conversion material. The energy gap below $^5D_4$ of $Tb^{3+}$ was so large (~15 000 $cm^{-1}$) that multiphonon emission relaxation can be neglected.

In this study, by increasing the dopant concentration of $Eu^{3+}$ (up to 20 mol%) and component of $(NH_4)_6Mo_7O_{24}\cdot 4H_2O$ (exceed the stoichiometric ratio 30%) in the synthesis, two one-phonon sidebands $PSB_1 = 449$ nm and $PSB_2 = 429$ nm associated with the $Eu^{3+}$ $^7F_0 \rightarrow {}^5D_2$ excitation transition at 464 nm (ZPL) were observed in the excitation spectra monitoring the $Eu^{3+}$ $^5D_0 \rightarrow {}^7F_2$ emission at 613 nm. The average phonon energy involved in the sideband formation were $\hbar\omega_{L1} = 612$ $cm^{-1}$ and $\hbar\omega_{L2} = 1077$ $cm^{-1}$. Furthermore, the phonon densities of states $\rho(\omega)$ were determined experimentally from the profile of one-phonon sideband. It was also important to study the phonon-impurity and phonon–phonon interactions.

## Experiment section

### Materials

For the combustion synthesis of $La_{1.6}Mo_2O_9:Eu_{0.4}{}^{3+}$, $La_2O_3$ (99.99%), $Eu_2O_3$ (99.99%), $(NH_4)_6Mo_7O_{24}\cdot 4H_2O$ (AR) and citric acid (AR), and for the preparation of β-$NaGdF_4:Tb^{3+}$ nanocrystals by a hydrothermal method, $Gd(NO_3)_3\cdot 6H_2O$, NaCl, $Tb(NO_3)_3\cdot 7H_2O$, $Er(NO_3)_3\cdot 5H_2O$, $Gd(NO_3)_3\cdot 6H_2O$, and $Tb(NO_3)_3\cdot 7H_2O$ were all used as received without additional purification or treatment.

### Synthesis

Powder of 20 mol% $Eu^{3+}$ ion-doped rare earth molybdates $La_2Mo_2O_9$:Eu was prepared by using a combustion method.[18] According to the stoichiometric ratio, $1.96 \times 10^{-2}$ mol $La_2O_3$ (99.99%), $0.4 \times 10^{-2}$ mol $Eu_2O_3$ (99.99%) and $HNO_3$ (analytical reagent, AR) was mixed under vigorous stirring, and the pH value of the solution was adjusted to 2–3 by dilute $NH_3\cdot H_2O$, the mixing materials were combusted at a moment, and the white powders were obtained. Then, $0.29 \times 10^{-2}$ mol $(NH_4)_6Mo_7O_{24}\cdot 4H_2O$ (AR) as well as 30 mL of a water–ethanol solution (volume ratio of water and ethanol is 1 : 8) of $4 \times 10^{-2}$ mol citric acid (AR) were added to the solution. The molar ratio of metal ions to citric acid was 1 : 2. The mixing solution was heated using an electric oven. After all the water was evaporated, the products were annealed at 500–900 °C for 2 h in air to get the final products.

The serial samples of β-$NaGdF_4:Tb^{3+}$ 1 mol% NCs were prepared by a hydrothermal method using a Span 80 template. A total of 30 mL of 1-butanol, 20 mL of water, and 4.5 mL of Span 80 were mixed and stirred for 10 min. This solution was divided into two parts: in one part, a solution mixture of 0.42 M of $Gd(NO_3)_3\cdot 6H_2O$ and 0.42 M of NaCl, as well as the required amount of $Tb(NO_3)_3\cdot 7H_2O$ and $Er(NO_3)_3\cdot 5H_2O$ were added and stirred for 10 min. 1.7 M solution of $NH_4F$ was added to another part of the solution and stirred for 5 min. Finally, the two solutions were combined and this mixture was put into a Teflon-lined stainless steel autoclave and maintained at 170 °C for 2 h. In this preparation technique, the $Ln^{3+}/F^-$ ratio and pH were maintained at 1 : 4 and 6 : 7, respectively. The NC sizes of β-$NaGdF_4:Tb^{3+}$ were controlled by the synthesis temperature (170 °C), concentrations (1.7–3.4 M) and pH values (5–7) with NaOH.

### Apparatus

Powder X-ray diffraction (XRD) measurements were carried out using a Bruker D8 advanced powder diffractometer with Cu Kα radiation ($\lambda = 1.54056$ Å) as the incident beam. The patterns were collected at room temperature with a $2\theta$ range of 10–80° for $La_2Mo_2O_9$: 20 mol% Eu and 10–70° for β-$NaGdF_4:Tb^{3+}$ 1 mol%. The morphology and particle size of the final products were characterized with a TEM (Technai T12). A sunlight (optical parametric oscillator, OPO) laser was used as the excitation source. A TDS 3052 digital phosphor oscilloscope was used to record the luminescence decay curves. The fluorescent lifetimes were measured by monitoring the $Tb^{3+}$ emission at 383 nm ($^5D_3 \rightarrow {}^7F_6$), excited by 273 nm ($Gd^{3+}$ $^8S_{7/2}$–$^6I_J$). The decay signals were processed by a Boxcar Averager (Model 162).

The excitation spectra were obtained using a Hitachi F-7000 fluorescence spectrophotometer equipped with a 150 W xenon lamp as the excitation light source. The scan speed was 240 nm $min^{-1}$, and the slit width was 1.0 nm.

## Results and discussions

### Characterization and measurements

From the powder XRD patterns (Fig. 1), we find that the $La_2Mo_2O_9$:Eu phosphors are pure phase and well-crystallized. $La_2Mo_2O_9$:Eu can be indexed to JCPDS 028-0509. No phase transition occurs through the annealing temperatures (500–900 °C), but when the annealing temperature decreases, the profiles of the peaks broaden and the intensity diminishes. The XRD patterns of β-$NaGdF_4:Tb^{3+}$ are shown in Fig. 2. Moreover, it is evident that the widths of the XRD peaks change with the size of samples. For the accurate determination of size, transmission electron microscopy (TEM) measurements were performed (Fig. 3). The histograms derived from Fig. 3 are shown in Fig. 4. The average particle sizes were found to be $d = 4.7$, 56.0 and

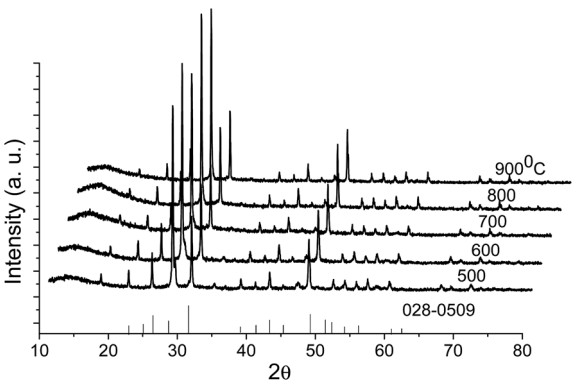


Fig. 1 XRD patterns of $La_2Mo_2O_9:Eu^{3+}$.

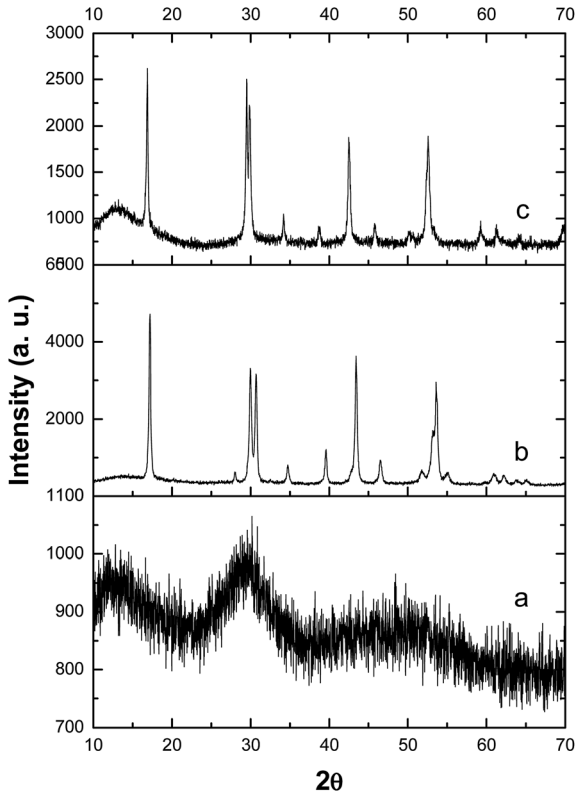


Fig. 2 XRD patterns of β-$NaGdF_4$:$Tb^{3+}$ nanocrystals.

115.5 nm, which is in good agreement with those obtained from the Scherrer's formula.

### One-phonon sideband

The $Eu^{3+}$ ion is a well-known spectroscopic probe to estimate the local environment in various crystals and glasses due to its simple energy level structure, *i.e.*, the $^7F_0$ ground and the $^5D_0$ excited states of $Eu^{3+}$ ion are singles and non-degenerate under any symmetry. The energy level diagram depicting the PSB process is shown in Fig. 5. The excitation spectra (Fig. 6) were obtained by monitoring the $Eu^{3+}$ $^5D_2 \rightarrow {}^7F_0$ emission at 613 nm. If the energy difference between the bonding and antibonding orbitals of the Mo–O groups is equal to the energy of charge transfer band of the $Eu^{3+}$ ions, the energy can be transferred from Mo–O groups through the charge transfer state to the 4f energy levels of $Eu^{3+}$ ions nonradiatively. From the emission spectra under excitation at 290 nm, Fig. 7, we can observe the energy transfer from Mo–O to the 4f energy levels of $Eu^{3+}$ ions.

The theory of transition of multiphonon and relaxation of lattice is found in the following approximation:[1–20]

(1) A single frequency approximation or both the parabolas of initial and final states have the same phonon energy, $\hbar\omega$.

(2) In the golden rule integration over the $z$ coordinate, the condon approximation is used.

(3) The transition taking place with the vibrational states of the initial parabola is in thermal equilibrium with the host. The Huang–Rhys–Pekar $W_p(S, \langle m\rangle)$ function is given by[31–34]

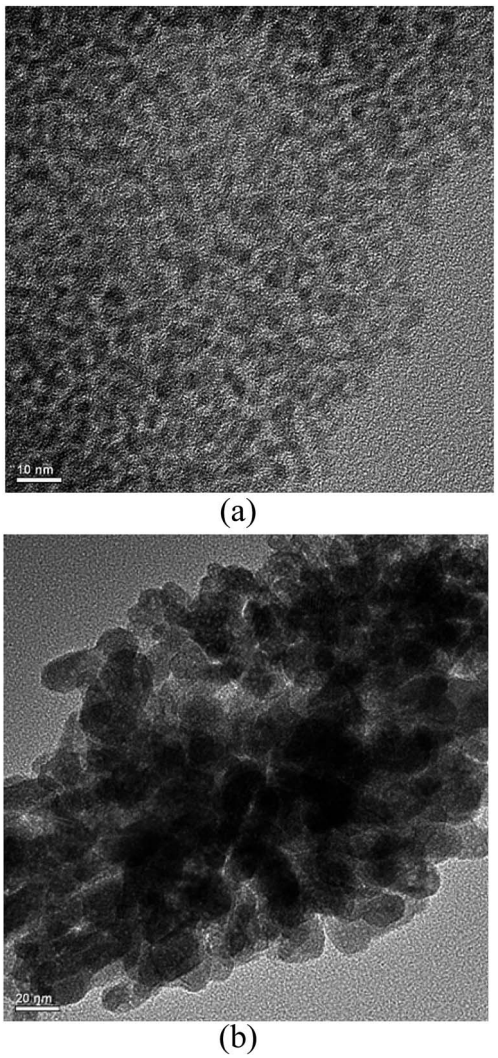


Fig. 3 TEM images of β-$NaGdF_4$:$Tb^{3+}$ nanocrystals, (a) $d = 4.7$ nm; (b) $d = 56.0$ nm.

$$W_p(S, \langle m\rangle) = e^{-S\langle 1+2m\rangle} \sum_{j=\max(0,-p)} \frac{(S\langle m\rangle)^j (S\langle 1+m\rangle)^{p+j}}{(p+j)!j!} \quad (1)$$

where $S$ is the Huang–Rhys factor, the parameter $\langle m\rangle = r/(1-r)$ is Planck's average thermal occupancy and $r = \exp(-\hbar\omega/kT)$ is the normalized thermal weight of the initial vibrational state. In addition, the Huang–Rhys factor can be calculated according to eqn (2).

$$S = \frac{I_{PSB}}{I_{ZPL}} = \frac{W_1(S, \langle m\rangle)}{W_0(S, \langle m\rangle)} = \begin{cases} S\langle 1+m\rangle; & P \geq 0; \\ S\langle m\rangle; & P < 0; \end{cases} \quad (2)$$

where $I_{PSB}$ and $I_{ZPL}$ are the integral intensity of PSB and ZPL, respectively. $P \geq 0$ is for the absorption of phonons and $p < 0$ is for the emission of phonons. Any radiative transition between electronic levels of an ion in a crystal will exhibit emission and absorption sidebands due to the perturbation. These sidebands correspond to the simultaneous emission or absorption of phonons, which occur due to the mixing of state functions *via* the perturbation. The $^7F_0 \rightarrow {}^5D_2$ 464 nm transition, namely the

 

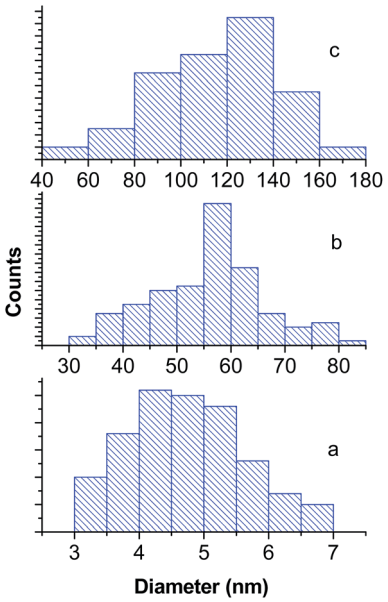


Fig. 4 Histograms of (a) sample a ($d = 4.7$ nm); (b) sample b ($d = 56.0$ nm) and (c) sample c ($d = 115.5$ nm).

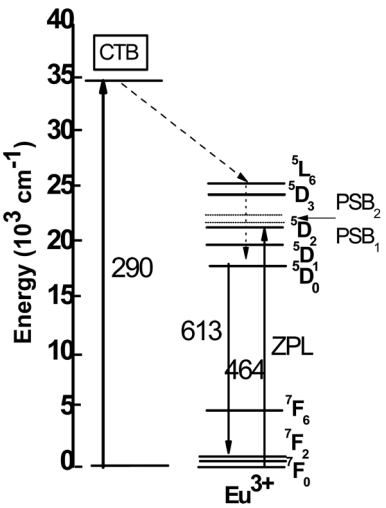


Fig. 5 Energy level and mechanism scheme depicting the PSB process of $La_2Mo_2O_9$:Eu.

ZLP, is a purely electric dipole transition, according to transition selection rules shown in Fig. 8 (a part of Fig. 6). Two PSBs located at 449 and 429 nm at the high energy side of the ZPL were observed. They result from the simultaneous excitation of the electronic transitions of $Eu^{3+}$ and of the vibrational modes around the dopant ion. The frequency gap $\Delta$ between the zero-phonon line and the peak of the phonon side band is determined by Franck–Condon principles. The two PSBs are due to the local mode arising from the Mo–O and O–Mo–O vibrations. This is a process of phonon absorption, therefore, $p \geq 0$ in eqn (2). In addition, $\langle 1 + m \rangle$ can also be approximately set as 1 because of higher phonon energy at room temperature. Therefore, the Huang factor can also be expressed as the ratio of the

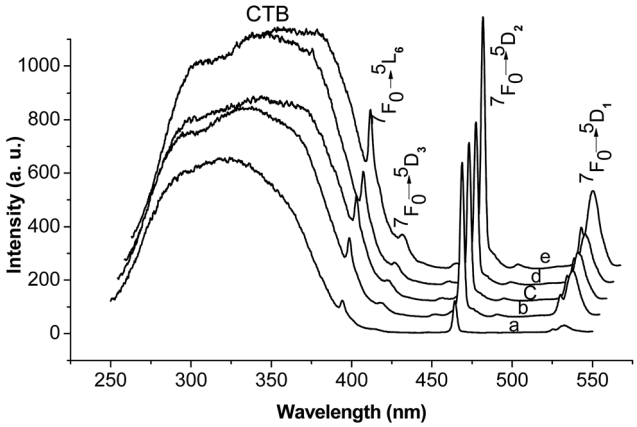


Fig. 6 Excitation spectra monitoring the $Eu^{3+}$ $^5D_2 \rightarrow {}^7F_0$ emission at 613 nm, a–e lines correspond the annealing temperatures at 500, 600, 700, 800 and 900 °C, respectively.

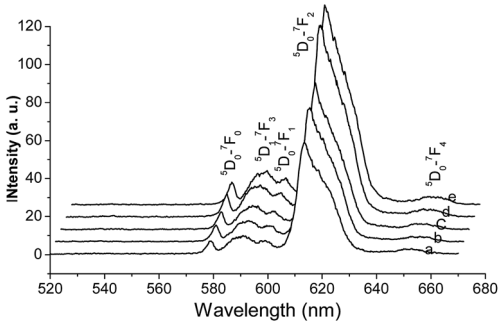


Fig. 7 Emission spectra of $La_2Mo_2O_9$:$Eu^{3+}$ under excitation at 290 nm in CTB, a–e lines correspond the annealing temperatures at 500, 600, 700, 800 and 900 °C, respectively.

integral intensity of the one-phonon line and zero-phonon line $I_{PSB}/I_{ZPL}$ (see eqn (1)), then $S_1 = 0.055$ and $S_2 = 0.037$. It is indicated that when the strength of the electron–phonon coupling is weak ($S < 1$) we have an intense ZPL in the spectrum, in contrast, when coupling is strong, the zero-phonon line is plunged in the multiphonon structure and cannot be separated. The profile of one-phonon PSB should be proportional both to the phonon density of states $\rho(\omega)$ and the probability of

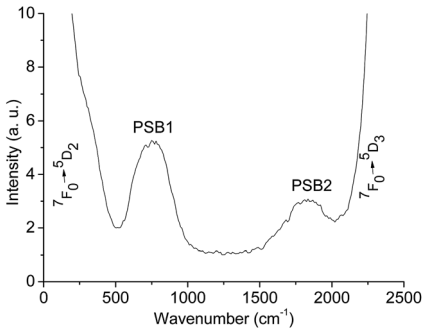


Fig. 8 Excitation spectrum monitoring the $Eu^{3+}$ $^5D_2 \rightarrow {}^7F_0$ emission at 613 nm, part of e-line in Fig. 6.

absorbing a phonon. An exact integrated relationship between the density of the phonon states and the shape of the phonon sideband in the general case of multiphonon transitions was obtained[21]

$$I(\omega, T) = \exp[-S(T)]\rho(\omega, T) + \frac{1}{\omega}\int_{-\infty}^{\infty} \rho(\omega, T)tI(\omega - t, T)\mathrm{d}t, \quad (3)$$

where $I(\omega,T)$ is the function describing the shape of the phonon band. If one neglects the integral term corresponding to the multiphonon transitions, the shape of the one-phonon sideband can be given as

$$I_1(\omega) = \exp(-S)\rho(\omega). \quad (4)$$

With the $S$ values above calculated, the phonon density of states $\rho(\omega)$ resulting from the impurity–phonon interaction can be determined and plotted, as shown in Fig. 9. The profile of one-phonon PSB can be described well by both Gaussian and Lorentzian shapes in Fig. 9. The full width at half maximum (FWHM) of the profile phonon sideband can be given as FWHM $= 2[2\ln 2S(\hbar\omega_L)^2]^{1/2}$, from which the average energy of the phonons $\hbar\omega_L$ involved in the sideband formation can be derived, $\hbar\omega_{L1} = 612\ \mathrm{cm}^{-1}$ and $\hbar\omega_{L2} = 1077\ \mathrm{cm}^{-1}$.

### MR of the $^5D_3 \rightarrow {}^5D_4$ of $Tb^{3+}$ in β-$NaGdF_4$:$Tb^{3+}$ NCs

Nonradiative transition is highly important in the study and design of devices of luminescence and lasing, because the competition between nonradiative transition and radiative transition decides the luminescence efficiency. Materials doped with rare-earth ions are important in luminescence and lasing materials. Therefore, the nonradiative transition of rare-earth ions has attracted considerable attention. The radiative transition probability of rare-earth ions (or intensity of spectral lines) can be calculated by applying the Judd–Ofelt theory.[22,23] The theory of nonradiative transition of rare-earth ions has been investigated.[24–31] The linear theory of Miyakawa and Dexter predicts an exponential energy-gap law, but is only valid for strong and intermediate electron–phonon coupling. A modified exponential energy-gap law reconciles the large variation in the exponential factor for transitions, involving only a few phonons. The nonlinear theory of Pukhov and Sakun[26] is valid for weak electron–phonon coupling, harmonic lattice vibrations, and a single phonon frequency model. This theory also has the advantage of expressing the MR rates in terms of the reduced matrix elements $\langle J'\|U^{(k)}\|J\rangle$ from the Judd–Ofelt theory. The lack of theory adequately copes with the MR rates observed for transitions, involving a large number of phonons ($n > 3$).[31] To date, some phenomenological formulas are still applied to estimate nonradiative transition experiments. For lanthanide ($Ln^{3+}$)-doped nanocrystals (NCs), confinement effects are induced mostly through electron–phonon interactions despite the localized 4f states. Thus, investigating the nonradiative transition, especially the MR of rare-earth ions, involving large energy gaps is important. Any property of NCs that depends on the vibrational spectrum, such as its thermodynamic properties or electron–phonon dynamics, is different at low energies than in bulk crystals. This phenomenon is especially true for NCs, for example, only weak coupling occurred in their surroundings in powder form.

This section mainly investigated the MR of NCs doped with rare-earth ions and compared it with that in the corresponding bulk material. The emission spectra excited by 273 nm ($Gd^{3+}$ $^8S_{7/2}$–$^6I_J$) and luminescence lifetimes of $^5D_3$–$^7F_6$ transition of $Tb^{3+}$ were measured at 12 K to 312 K, and MR rates for the $^5D_3 \rightarrow {}^5D_4$ of $Tb^{3+}$ in β-$NaGdF_4$:$Tb^{3+}$ NCs were calculated. The temperature dependence of MR rates for the $^5D_3 \rightarrow {}^5D_4$ were analyzed by single-frequency approximation in the framework of the nonlinear theory of MR. The luminescent process in β-$NaGdF_4$:$Tb^{3+}$ started with excitation of the $Gd^{3+}$ ion (273 nm, $^8S_{7/2}$–$^6I_J$), and then energy migration among the inner lattices of $Gd^{3+}$ occurred until the excitation energy was trapped by the activator ions $Tb^{3+}$, from which emissions occurred. The emission spectra of samples were measured at seven temperatures($T$= 12 K to 312 K). The emission spectra at 12 K, 162 K and 312 K are given in Fig. 10. The $^5D_4$–$\sum{}^7F_J$ ($J$ = 3, 4, 5, 6) transitions were predominant in the emission spectra.

Temperature-dependent contributions to fluorescence lifetimes come from: (i) the thermal population of nearby emitting levels (ii) vibrational 4f–5d, (iii) J-mixings and (iv) multiphonon emission processes. Because the energy gap between $^5D_3$ and $^5D_4$ is much larger than $kT$, the temperature variations of lifetimes of the $^5D_3$- and $^5D_4$-emissions are caused mainly by the first three processes. Therefore, the observed lifetimes showed relatively small and complicated temperature-variations. The luminescent decay curves of $^5D_3$–$^7F_6$ transition (383 nm) were fitted with the single exponential functions as shown in Fig. 11, and tabulated in Table 1.

The multiphonon emission process of $^5D_3$–$^5D_4$ sometimes became a dominant mode of decay of the $^5D_3$ state. The magnitude of static and vibrational crystal field acting on $Tb^{3+}$ influenced the degree of the 4f–5d mixing and J-mixing, as well as the radiationless transition rates.

A rare-earth ion in an excited state $i$ decays with a lifetime $\tau_i$ given by

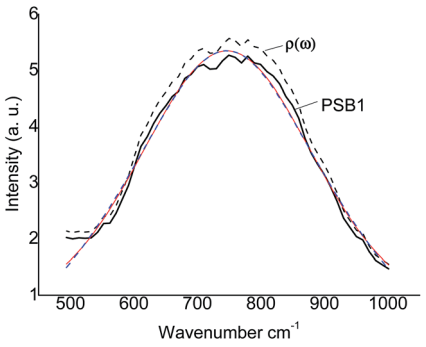


Fig. 9 The phonon density of states $\rho(\omega)$ and the fit curves by Gaussian (red line) and Lorentzian (blue-dashed line) line shapes of PSB1. The $x$-axis is the distance from the center (set as 0) of $Eu^{3+}$ $^7F_0 \rightarrow {}^5D_2$ excitation peak.

 

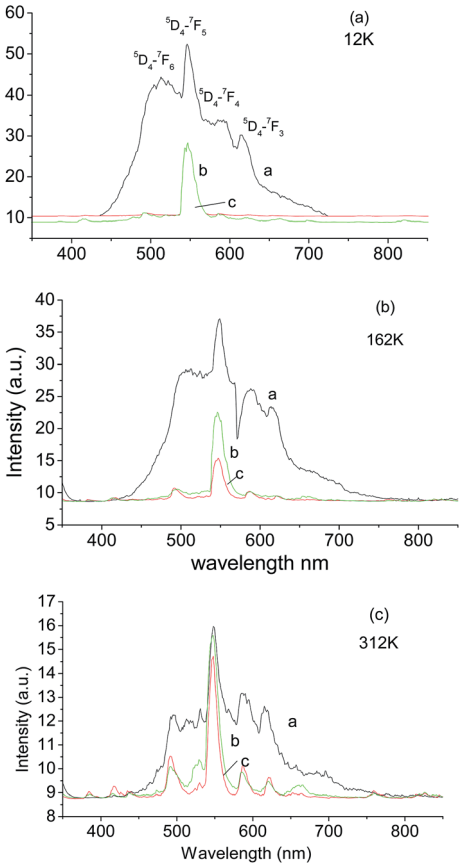


Fig. 10 Emission spectra of (a) sample a ($d$ = 4.7 nm); (b) sample b ($d$ = 56.0 nm) and (c) sample c ($d$ = 115.5 nm) excited by 273 nm ($Gd^{3+}$ $^8S_{7/2}$–$^6I_J$).

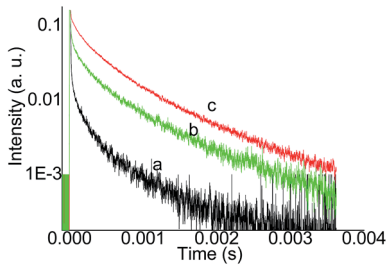


Fig. 11 Decay curves of $Tb^{3+}$ $^5D_3$–$^7F_6$ transition (383 nm) of samples a–c at $T$ = 12 K.

$$\frac{1}{\tau_i} = \sum_j \left(A_{ij} + W_{ij}\right) = \Gamma_{\mathrm{ir}} + \Gamma_{\mathrm{inr}}, \tag{5}$$

where $A_{ij}$ and $W_{ij}$ are the rates for radiative and nonradiative decays, respectively, and the summation is over all terminal states $j$. MR processes are sometimes the dominant modes of relaxation of 4f-states. The probability of spontaneous multiphonon emission increases as the energy gap decreases. The probability also depends on the energies of phonons and the densities of their states. The excitation energy is always supplied to $^5D_4$ through $^5D_3$ in host lattices with a large forbidden gap in the case of the 4f–5d band excitation. The multiphonon emission process of $^5D_3 \rightarrow {}^5D_4$ sometimes becomes a dominant mode of decay of the $^5D_3$ state. As a result, the $^5D_4$-emission owes its intensity to the $^5D_3 \rightarrow {}^5D_4$ relaxation rates. This rate of multiphonon emission process of $^5D_3 \rightarrow {}^5D_4$, $\Gamma_{\mathrm{nr}}$ is obtained using the following relation:[12]

$$\Gamma_{\mathrm{nr}} = \Gamma(^5\mathrm{D}_3)\frac{I_4}{(I_3 + I_4)} \tag{6}$$

where $\Gamma(^5D_3)$ is the reciprocal of the observed fluorescence lifetime of $^5D_3 \rightarrow {}^7F_J$, and $I_3$ and $I_4$ are total quantum outputs of the $^5D_3$- and $^5D_4$-emissions, respectively. The MR rates of $^5D_3 \rightarrow {}^5D_4$ at various temperatures were derived from eqn (5), see Table 1.

The temperature dependence of nonradiative transition rates is usually explained by the multiphonon process of a single phonon mode, as performed in ref. 24–33. The phonons of various modes may be involved in the $^5D_3$–$^5D_4$ relaxation. Moreover, the variation of thermal population of the levels near $^5D_3$ makes the temperature dependence further complicated. Thus, the $^5D_3$–$^5D_4$ nonradiative relaxation rates caused by spontaneous multiphonon emission strongly depend on the vibrational properties of matrices.

The phonon energies covering the $^5D_3$–$^5D_4$ energy gap ($\sim$5800 $cm^{-1}$) must be considerably large to minimize the order of the multiphonon process. Because the density of such phonons available is low at room temperature and below, the observed nonradiative transition probabilities are considered almost as those of the spontaneous multiphonon emission. If $n$ is the smallest integer such that $n\hbar\omega_{\max} \geq \Delta E = 5800\ \mathrm{cm}^{-1}$, one assumes that

$$W(T) = W(0)[1 - \exp(-\Delta E/k_{\mathrm{B}}T)]^{-n}. \tag{7}$$

Eqn (7) was used to describe the temperature dependence of MR rate.[25–29] However, when the energy gap $\Delta E$ became larger, for example, $\Delta E = 5800\ \mathrm{cm}^{-1}$, the factor $\exp(-\Delta E/k_{\mathrm{B}}T) \rightarrow 0$ rapidly with temperature $T$ from 12 K to 350 K. The experiment showed that in the case of weak electron–phonon coupling, multiphonon nonradiative transition probability $\Gamma_{\mathrm{nr}}(T)$ decreased rapidly with increasing order $n = \Delta E/\hbar\omega$ of the process, or normalized energy gap. The phonon modes in the narrow range near the highest frequency (cutoff frequency) of the phonon spectrum contributed greatly to $\Gamma_{\mathrm{nr}}(T)$, because they conserved energy in the lowest-order process.[23] As a result, for relaxation by the emission of phonons of a single frequency $\omega$, where $\omega \approx \omega_{\max} = \omega_{\mathrm{co}}$, the order of the process required to bridge an energy gap $\Delta E$ is $n = \Delta E/\hbar\omega$. The nanostructure dimensions eliminate the low-frequency vibrations, providing a cutoff in the phonon density-of-states that depends on particle size. The size-resonant spherical and torsional modes dominate near the cutoff. The main peak positions are 291, 356, and 401 $cm^{-1}$ for $NaGdF_4$ NCs in the micro-Raman spectra.[24]

If the temperature is not very high and the Huang–Rhys parameter $S$ is very small ($S \ll 1$), the temperature dependence for an $n$-phonon process using single-frequency model is given by:[31–33]

$$\Gamma_{\mathrm{nr}}(T) = \Gamma_{\mathrm{nr}}(0)\left[\frac{1}{\exp(\hbar\omega/k_{\mathrm{B}}T) - 1} + 1\right]^{\Delta E/\hbar\omega} \tag{8}$$

Table 1 The experimental data and parameters of the $^5D_3$–$^7F_6$ transition of $Tb^{3+}$ in β-$NaGdF_4$ NCs at various temperatures

| | | Temp. (K) | | | | | | |
|---|---|---|---|---|---|---|---|---|
| Sample | | 12 | 62 | 112 | 162 | 212 | 262 | 312 |
| $\tau$ (μs) | a | 170 ± 5.4 | 160 ± 4.0 | 150 ± 0.34 | 90 ± 0.07 | 69 ± 0.02 | 31 ± 0.03 | 14 ± 0.003 |
| | b | 460 ± 0.1 | 455 ± 0.1 | 453 ± 0.1 | 375 ± 0.1 | 286 ± 0.7 | 82 ± 0.1 | 55 ± 0.2 |
| | c | 500 ± 8.3 | 495 ± 5.3 | 490 ± 0.2 | 362 ± 6.2 | 305 ± 0.8 | 123 ± 1.6 | 67 ± 0.9 |
| $\Gamma$ ($s^{-1}$) | a | 5882 | 6250 | 6667 | 11 111 | 14 534 | 31 958 | 71 923 |
| | b | 2174 | 2198 | 2208 | 2667 | 4237 | 12 195 | 18 182 |
| | c | 2000 | 2020 | 2041 | 2762 | 3279 | 8130 | 14 925 |
| $I_4/(I_3 + I_4)$ | a | 0.81 | 0.78 | 0.81 | 0.82 | 0.84 | 0.86 | 0.88 |
| | b | 0.66 | 0.69 | 0.67 | 0.68 | 0.69 | 0.73 | 0.82 |
| | c | 0.69 | 0.69 | 0.69 | 0.71 | 0.77 | 0.79 | 0.81 |
| $\Gamma_{nr}$ ($s^{-1}$) | a | 4764 | 4875 | 5400 | 9111 | 12 209 | 27 484 | 63 292 |
| | b | 1435 | 1517 | 1479 | 1813 | 2924 | 8902 | 14 909 |
| | c | 1380 | 1394 | 1408 | 1961 | 2525 | 6423 | 12 089 |

where $\Gamma_{nr}(0)$ is the spontaneous emission probability at $T = 0$ K, take $\Gamma_{nr}(0) = \Gamma_{nr}(12\ K)$, $\hbar\omega = \hbar\omega_{co} = 401\ cm^{-1}$. Fig. 12 shows that the experimental data agreed well with the theoretical curves; moreover, the temperature dependence of MR rates is described well by the model.

To avoid energy transfer and cross-relaxation processes, the doping concentration of $Tb^{3+}$ in β-$NaGdF_4$ NC samples were limited to 1 mol%. Given that the nonradiative channels increase, the luminescence efficiencies reduce for the small NCs. The enlargement of the local field is considered an effective approach to enhance luminescence efficiency because the overall luminescence efficiency of the system depends on the ratio between the radiative and nonradiative lifetimes.

In conclusion, the normal modes of vibration of a perfect lattice, modified by the substitutional impurity ($Eu^{3+}$) defects were investigated. These modes are not travelling plane waves as those of the perfect lattice but rather vibrational modes centered at the defects with the amplitude of vibrational exponentially attenuating with distance from the impurity. The two PSBs resulted from the localized modes were observed. The average energy of the phonons $\hbar\omega_L$ involved in the sideband formation were derived, $\hbar\omega_{L1} = 612\ cm^{-1}$ and $\hbar\omega_{L2} = 1077\ cm^{-1}$.

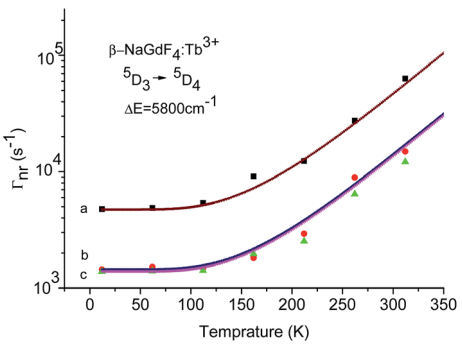


Fig. 12 Temperature dependence of MR rates of samples a (experimental data-black square, fitted curve by eqn (8) – red line); b (experimental data-red square, fitted curve by eqn (8) – blue line) and c (experimental data-green triangle, fitted curve by eqn (8) – pin line).

The intensity of PSB is Poisson-distributed $I = e^{-S}(S^n/n!)$, with $S$ being the Huang–Rhys factor and $n$ the number of phonon replicas. The intensity ratio of one- and two-phonon sidebands is $I_2/I_1 = S/2 \ll 1$. Therefore, only one-phonon PSB can be observed in rare earth dopant materials ($s < 1$).

The MR rates of $Tb^{3+}$ $^5D_3 \rightarrow {}^5D_4$ were determined from the emission spectra and fluorescence decays at different temperatures. The nanostructure dimensions eliminated the low-frequency vibrations, providing a cutoff in the phonon density of states that depends on particle size. The $\omega_{max}$ value of 401 $cm^{-1}$ was selected as the cutoff frequency $\omega_{co}$. In the MR of the RE ions, the phonons with $\hbar\omega_{max}$ play an important role. Because the numbers connecting the energy gap $\Delta E$ needed to emit are $N = \Delta E/\hbar\omega_{max}$. It is evident that the $N_{min}$ only corresponds to the phonons $\hbar\omega_{max}$. The smaller $N$ is, the larger the transition probability is, which means that the transition probability is the best large for the phonons $\hbar\omega_{max}$. The experimental data agreed with the theoretical curves in the analysis for temperature dependences of the MR rates of $^5D_3 \rightarrow {}^5D_4$. The MR occurred predominantly through high-energy optical phonons.

## Acknowledgements

The authors are grateful to the National Natural Science Foundation of China (NSFC) (nos 61077025, 10904140, 10774142 and 60308008) for support.

## References

1 M. J. Weber, *Phys. Rev. B: Solid State*, 1973, **8**, 54–64.
2 M. D. Sturge, *Phys. Rev. B: Solid State*, 1973, **8**, 6–14.
3 H. Dubost, L. Abouaf-Maguin and F. Legay, *Phys. Rev. Lett.*, 1973, **22**, 145–148.
4 G. Zhang, X. Ying, L. Yao and H. Chen, *J. Lumin.*, 1994, **59**, 315–320.
5 U. Happek, C. E. Mugan, W. von der Osten and A. J. Sievers, *Phys. Rev. Lett.*, 1994, **72**, 3903–3906.

 

6 M. P. Miller and J. C. Wright, *J. Chem. Phys.*, 1979, **71**, 324–338.
7 K. Huang and A. Rhys, *Proc. R. Soc. London, Ser. A*, 1950, **204**, 406–426.
8 C. W. Struck and W. H. Fonger, *J. Lumin.*, 1975, **10**, 1–30.
9 K. Huang, *Progr. Phys.*, 1981, **1**, 31–85.
10 W. Y. Jia, R. T. Brundage and W. M. Yen, *Phys. Rev. B: Condens. Matter Mater. Phys.*, 1983, **27**, 41–45.
11 Y. Tian, X. H. Qi, X. W. Wu, R. N. Hua and B. J. Chen, *J. Phys. Chem. C*, 2009, **113**, 10767–10772.
12 S. Neeraj, N. Kijimaand and A. Cheetham, *Chem. Phys. Lett.*, 2004, **387**, 2–6.
13 J. A. Alonso, F. Rivillas, M. J. Matinez-Lope and V. Pomjakushin, *J. Solid State Chem.*, 2004, **177**, 2470–2476.
14 H. Li, S. Zhang, S. Zhou, X. Cao and Y. Zheng, *J. Phys. Chem. C*, 2009, **113**, 13115–13120.
15 H. Liu, R. A. Secco, N. Imanaka and G. Adachi, *Solid State Commun.*, 2002, **121**, 177–180.
16 S. Sumithraa, A. K. Tyagib and A. M. Umarjia, *Mater. Sci. Eng., B*, 2005, **116**, 14–18.
17 D. A. Woodcock, P. Lightfoot and C. Ritter, *J. Solid State Chem.*, 2000, **149**, 92–98.
18 C. X. Liu, J. Y. Liu and K. Dou, *J. Phys. Chem. B*, 2006, **110**, 20277–20281.
19 G. Blasse, *Int. Rev. Phys. Chem.*, 1992, **11**, 71–100.
20 S. I. Pekar, *J. Exp. Theor. Phys.*, 1950, **20**, 510–523.
21 R. H. Bartram, *J. Phys. Chem. Solids*, 1990, **51**, 641–651.
22 B. R. Judd, *Phys. Rev.*, 1962, **127**, 750–761.
23 C. S. Ofelt, *J. Chem. Phys.*, 1962, **37**, 511–520.
24 A. Riseberg and H. W. Moos, *Phys. Rev. Lett.*, 1967, **19**, 1423–1425.
25 T. Miyakawa and D. L. Dexter, *Phys. Rev. B: Solid State*, 1970, **1**, 2961–2969.
26 K. K. Pukhov and V. P. Sakun, *Phys. Status Solidi B*, 1979, **95**, 391–402.
27 F. K. Fong, S. L. Naberhuis and M. M. Miller, *J. Chem. Phys.*, 1972, **56**, 4020–4027.
28 M. J. Weber, *Phys. Rev. B: Solid State*, 1973, **8**, 54–63.
29 L. A. Riseberg and M. J. Weber, in *Progress in Optics*, ed. E. Wolf, 1976, vol. 14, pp. 89–159.
30 S. A. Egrov and J. L. Skinner, *J. Chem. Phys.*, 1995, **103**, 1533–1542.
31 Y. Orlovskii, *Phys. Rev. B: Condens. Matter Mater. Phys.*, 1994, **49**, 3821–3830.
32 Z. Burshtein, *Opt. Eng.*, 2010, **49**, 091005.
33 S. Kuboniwa and T. Hoshina, *J. Phys. Soc. Jpn.*, 1972, **32**, 1059–1068.
34 M. Banski, A. Podhorodecki, J. Misiewicz, M. Afzaal, A. Abdelhadyc and P. O'Brienc, *J. Mater. Chem. C*, 2013, **1**, 801–807.